APPLIED SCIENCES AND ENGINEERING

Tuning conformation, assembly, and charge transport properties of conjugated polymers by printing flow

Kyung Sun Park[1]*, Justin J. Kwok[2]*, Rishat Dilmurat[3], Ge Qu[1], Prapti Kafle[1], Xuyi Luo[4], Seok-Heon Jung[5], Yoann Olivier[3], Jin-Kyun Lee[5], Jianguo Mei[4], David Beljonne[3], Ying Diao[1,2,6†]

Intrachain charge transport is unique to conjugated polymers distinct from inorganic and small molecular semiconductors and is key to achieving high-performance organic electronics. Polymer backbone planarity and thin film morphology sensitively modulate intrachain charge transport. However, simple, generic nonsynthetic approaches for tuning backbone planarity and the ensuing multiscale assembly process do not exist. We first demonstrate that printing flow is capable of planarizing the originally twisted polymer backbone to substantially increase the conjugation length. This conformation change leads to a marked morphological transition from chiral, twinned domains to achiral, highly aligned morphology, hence a fourfold increase in charge carrier mobilities. We found a surprising mechanism that flow extinguishes a lyotropic twist-bend mesophase upon backbone planarization, leading to the observed morphology and electronic structure transitions.

INTRODUCTION

Conjugated polymers have attracted intense interest for their numerous (opto)electronic and biomedical applications (*1*). Their optical and electronic properties are highly dependent on polymer conformation and multiscale morphology because charge transport relies on the delocalization of π-electrons along the polymer backbones (intrachain) and between the chains (interchain) (*2*). In particular, the planarization of the backbone can extend the effective π-conjugation length and enhance intrachain charge delocalization, which is essential for realizing disorder-free transport (*3*) and high charge carrier mobility (*4*). Molecular design has been most extensively applied for tuning backbone torsion and electronic structure (*5*, *6*). For example, noncovalent interactions such as chalcogen-chalcogen or hydrogen bonding interactions were designed to enforce backbone coplanarity in several cases (*7*, *8*). Besides synthetic approaches, there are physical, post-processing methods developed to enhance the planarity of conjugated polymers in already deposited films such as mechanical rubbing and applying a hydrostatic pressure on the order of gigapascals (*9*, *10*). However, simple and broadly applicable approaches for controlling backbone planarity and the ensuing multiscale assembly process have not been reported before.

Fluid flow remains a rarely explored method for modulating the conformation and thin film morphology of conjugated polymers despite their ubiquity across all solution processing techniques. On the other hand, flexible polymers (e.g., polyethylene) subjected to flow have been studied extensively because of the industrially relevant processing of plastics (*11*–*13*). In particular, the flow-induced crystallization of flexible polymers is well studied and can be predicted by the facilitating decrease in conformational entropy of polymer chains (*14*). This knowledge is not directly transferrable to semiflexible, structurally complex conjugated polymers. While recent studies alluded to or surmised the important role of processing flow in crystallization (*15*, *16*), microphase separation (*17*), and alignment of conjugated molecules (*18*, *19*), there is no prior report on flow-induced conformation change and flow-altered assembly pathways for conjugated polymers. Furthermore, mechanistic insights are generally absent on how flow influences the conformation and assembly of conjugated polymers.

Here, we first report an unexpected finding that printing flow is capable of planarizing the conjugated polymers, thereby altering liquid crystal–mediated assembly pathways to largely modulate their electronic properties. Twisted-to-planar molecular conformation change is accompanied by a marked morphological transition from chiral, zigzag twinned domains to achiral, highly aligned thin film morphology. The resulting higher conjugation length and backbone alignment lead to markedly enhanced field-effect mobility and charge transport anisotropy. We further elucidate that this drastic morphological transition originates from the removal of a twist-bend liquid crystal phase upon backbone planarization. Through this example, we show that flow-directed assembly, a phenomenon ubiquitous in additive manufacturing, offers untapped opportunities for modulating structure and properties of functional materials down to the molecular scale.

RESULTS AND DISCUSSIONS

We performed a combined experimental and simulation study to investigate the role of fluid flow on the molecular conformation and morphology of printed conjugated polymer films. We used meniscus-guided printing (MGP) methods, such as blade coating (*20*) and capillary pen writing (*21*), to print conjugated polymer films over a range of speeds (Fig. 1A). The donor-acceptor (D-A) copolymers used include an isoindigo-bithiophene–based polymer (PII-2T) (*5*) (as a primary system), a thieno-isoindigo-bithiophene–based polymer (PTII-2T) (*5*), a diketopyrrolopyrrole-benzotriazole–based polymer (DPP-BTz) (*22*), and a diketopyrrolopyrrole-thienothiophene–based polymer (DPP2T-TT) (*23*) (Fig. 1B). These were chosen because of their varying degrees of molecular planarity (discussed below) that can affect their solution state conformation, response to flow, and subsequent film morphology.

[1]Department of Chemical and Biomolecular Engineering, University of Illinois at Urbana-Champaign, 600 S. Mathews Ave., Urbana, IL 61801, USA. [2]Department of Materials Science and Engineering, University of Illinois at Urbana-Champaign, 1304 W. Green St., Urbana, IL 61801, USA. [3]Laboratory for Chemistry of Novel Materials, University of Mons, Place du Parc, 20, B-7000 Mons, Belgium. [4]Department of Chemistry, Purdue University, 560 Oval Dr., West Lafayette, IN 47907, USA. [5]Department of Polymer Science and Engineering, Inha University, 100 Inha-ro, Incheon 402-751, South Korea. [6]Beckman Institute, Molecular Science and Engineering, University of Illinois at Urbana-Champaign, 405 N. Mathews Ave., Urbana, IL 61801, USA.
*These authors contributed equally to this work.
†Corresponding author. Email: yingdiao@illinois.edu

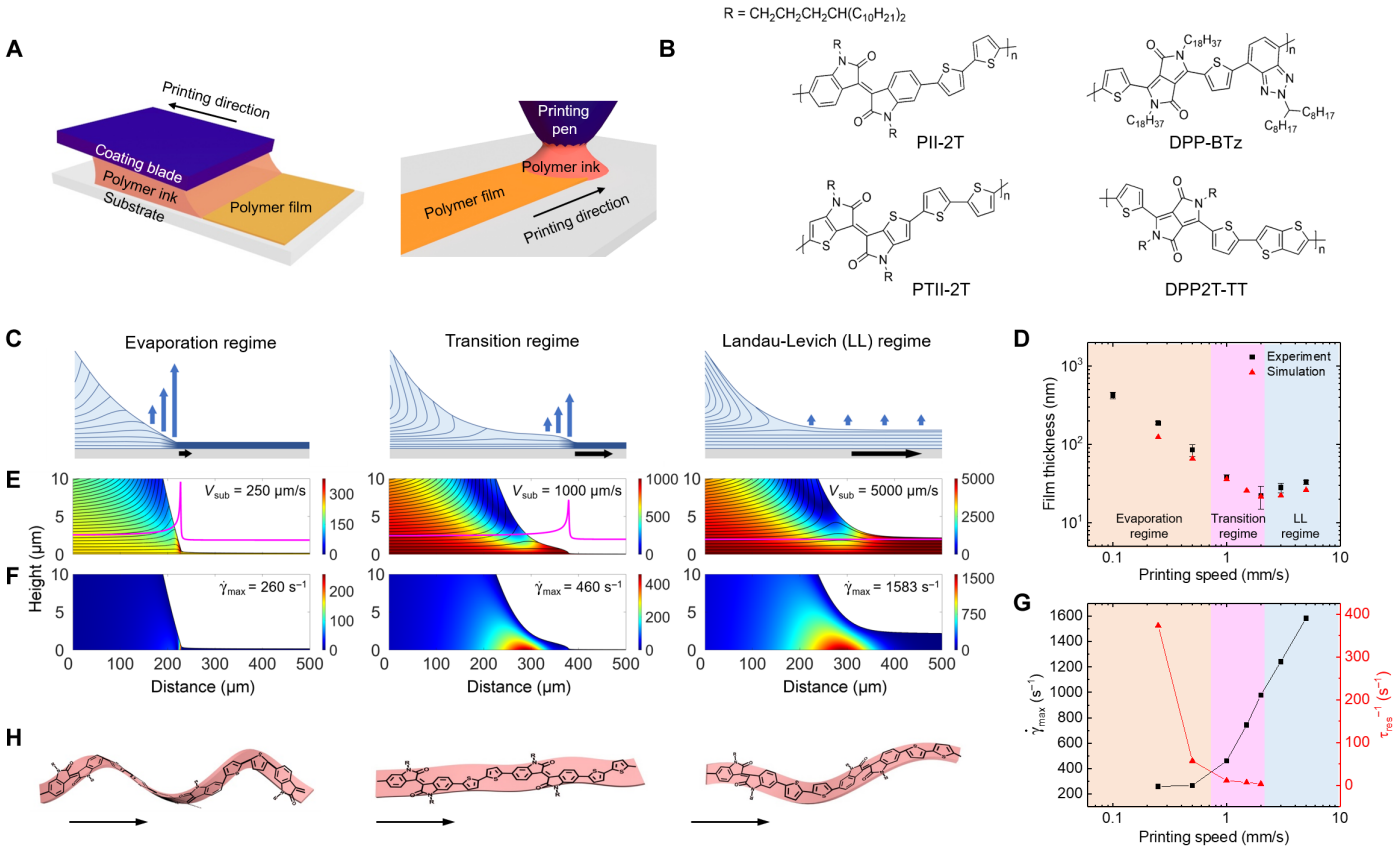

Fig. 1. Printing methods, model systems, and printing regimes. (**A**) Schematic of blade coating (left) and capillary pen writing (right) processes to produce conjugated polymer films. (**B**) Chemical structure of the four conjugated polymers used in this study. (**C**) Schematic illustration of the evaporation profile, flow field, and meniscus shape comparing the three printing regimes. (**D**) Comparison between experimentally measured (black squares) and simulated (red triangles) film thicknesses as a function of printing speed. Regions of the plot corresponding to evaporation, transition, and LL regimes are colored orange, pink, and blue, respectively. (**E**) Streamline representation of the flow field comparing three regimes; corresponding printing speeds (V_{sub}) are labeled. Evaporative flux profile is overlaid (magenta line), showing that the evaporation rate peaks at the contact line in the evaporation and transition regimes. (**F**) Strain rate ($\dot{\gamma}$) in the meniscus comparing three regimes at corresponding printing speeds; peak strain rates ($\dot{\gamma}_{max}$) are labeled. (**G**) Peak strain rate and inverse residence time (τ_{res}^{-1}) as a function of printing speed. Strain rate (black squares) begins to increase drastically in the transition regime because of increasing viscous forces. Residence time (red triangles) from the position of the maximum strain rate to the contact line is initially short in the evaporation regime and increases with increasing speed. Residence time remains relatively short and finite in the transition regime and then approaches infinity in the LL regime, allowing the relaxation of polymer orientation and conformation. (**H**) Schematic of PII-2T polymer conformation change across three regimes (see results below).

In MGP, flow arises from two main effects, capillary flow induced by solvent evaporation and viscous forces imposed by the blade or the substrate (*24*). It has been shown that the competition of these two driving forces gives rise to two deposition regimes: the evaporation regime and the Landau-Levich (LL) regime (*25*). In this work, we introduce a third regime, referred to as the "transition regime," occurring in between these two (Fig. 1C). These regimes can be characterized by their printing speed–dependent film thicknesses, flow profile, and meniscus shape. We identify the printing regimes by performing numerical simulations to model the multiphysical processes occurring in the meniscus considering fluid flow, solute convection-diffusion, and solvent vapor diffusion. A description of the simulation model and its sensitivity to certain parameters are shown in section S1 and fig. S1. To couple the physics, we apply a kinematic boundary condition at the meniscus-free surface that accounts for a solvent evaporative flux dependent on the solute concentration. This results in a contact line where the dilute solution becomes increasingly concentrated until becoming a nearly solidified film. The final set of governing equations is solved by the finite element method using the partial differential equation interface in COMSOL Multiphysics. Predictions of film thicknesses and regimes match well with those measured experimentally, indicating the successful modeling of the multiphysical processes in the meniscus that lead to film deposition (Fig. 1D). Figure 1E shows the plots of meniscus shape and velocity profile near the substrate for 0.25, 1, and 5 mm/s, corresponding to the evaporation, transition, and LL regimes, respectively, with the evaporative flux profiles overlaid on top (see figs. S2 and S3 for the full speed series). In the evaporation regime, solvent evaporation is dominant over the viscous forces imparted by the substrate resulting in a meniscus with nearly constant curvature up to the triple-phase contact line, indicating no viscous drag out at low printing speeds. In the transition regime, the curvature of the meniscus changes before the contact line because of the formation of a partially dragged out liquid film resultant from the increasingly non-negligible role of viscous forces with increased printing speed. Despite viscous drag out of the meniscus, solvent evaporation is still strong enough such that the contact

line exists in proximity to the meniscus at steady state, indicating that the contact line propagates along with the guided meniscus. At the same time, recirculation begins to occur in the meniscus because the solvent cannot evaporate fast enough. This recirculation produces a large "pocket" of high strain rate, which we believe is key to the morphological transition observed in the transition regime (shown below). With further increase in printing speeds, viscous forces dominate, while solvent evaporation becomes negligible and can no longer sustain a constant meniscus. As a result, the contact line is practically infinitely far away as a bulk liquid film is completely dragged out, followed by quiescent drying. The recirculation also becomes greater, resulting in a higher velocity gradient and therefore a larger strain rate. Figure 1F shows the total strain rate (magnitude of the strain rate tensor) for the three printing speeds evaluated from the velocity field and its spatial derivatives. In all cases, the strain rate tensor is dominated by shear with very small contributions of extension or compression except for a thin region near the free surface where tangential stress is zero. Therefore, in our discussion, strain rate is essentially equivalent to shear rate. The strain rate within the meniscus increases superlinearly with printing speed. At the same time, the residence time from the peak strain rate position to the contact line rises from nearly zero in the evaporation regime to infinity in the LL regime because of viscous drag out. The peak strain rate and inverse residence time are plotted versus printing speed (Fig. 1G). While the evaporation and LL regimes are characterized by strain rates and residence times that are both low and high, respectively, the transition regime is unique in that the strain rate begins to rise rapidly, while the residence time remains relatively low and finite so that flow-induced polymer conformation cannot fully relax. Notably, absolute values of strain rates may not exactly correspond to experimental values because of assumptions in several model parameters (table S1 and fig. S1). However, considering the good match in regimes between simulation and experiment (Fig. 1D), we believe that the trends in meniscus shape and flow profile are still valid. We subsequently show that the printing regimes have profound impact on the polymer conformation (Fig. 1H). In particular, the transition regime leads to the molecular scale planarization of the polymer backbone, mesoscale chiral-to-achiral transition of polymer fibril, and macroscale alignment of fibril aggregates. We believe that the transition regime presents an ideal condition where the strain rate is large enough to induce polymer conformation change and fibril alignment, but the residence time remains short enough to preclude conformational relaxation of the polymer and orientational relaxation of polymer aggregates.

The meniscus flow profile drastically modulated the multiscale morphology of printed films across the three regimes. At the molecular scale, the absorption coefficient (α) of PII-2T films measured by ultraviolet-visible (UV-vis) spectroscopy revealed distinct molecular conformations and electronic structures of conjugated polymers across regimes (Fig. 2, A and B). Considering that the printed films are anisotropic, we averaged the spectra of each film over multiple in-plane rotation angles to obtain the α values shown in Fig. 2 (A and B). The α value rises drastically as the printing speed increases from 0.1 to 1 mm/s, followed by a gradual decrease above 1 mm/s. We attribute the higher α value to the increased conjugation length of the polymer (*26*, *27*) in the transition regime (1 mm/s). Strictly speaking, the α values that directly correlate with conjugation length should be obtained from three-dimensional (3D) isotropic films. The α values we measured represent those of 2D isotropic films, which can be up to ~50% higher than the 3D isotropic case. Nonetheless, we observed an almost sixfold increase of α from 0.1 to 1 mm/s, which goes much beyond this possible error. To validate the inferred conformation change during regime crossing, we further performed quantum chemical calculations and surface-enhanced Raman spectroscopy (SERS). Our quantum chemical calculations show large torsional (~21°) angles between donor and acceptor units and intra-acceptor torsional angles (~11°) in the isoindigo unit as well for a geometrically optimized PII-2T structure (*5*) (shown below). We postulate that the twisted PII-2T chains are present in the films printed in the evaporation regime, showing relatively lower conjugation length and α values; because of the increased strain rate in the transition regime, the twisted PII-2T chains are planarized, resulting in higher conjugation lengths and therefore higher α values. The calculated absorption for varying lengths of PII-2T-repeating units shows enhanced intensity with increasing chain length and conjugation due to increased orbital overlap of the conjugated core (Fig. 2C and fig. S4). This result supports our hypothesis that higher optical absorption in films printed in the transition regime is due to the higher extent of π-electron delocalization from the planarized polymer backbone. Our hypothesis is also supported by the relative intensity of the vibronic progression in absorption, characterized by the absorption peak ratio ($A_{0\text{-}0}/A_{0\text{-}1}$), where 0-0 and 0-1 denote the purely electronic transition and a higher-energy vibronic replica, respectively. The values of $A_{0\text{-}0}/A_{0\text{-}1}$ are 1.07, 1.47, and 1.43 for films printed in the evaporation, transition, and LL regime, respectively (fig. S7). As this ratio measures the magnitude of the polaron relaxation energy that scales inversely with excitation delocalization and chain planarization, we conclude that the π-conjugation is maximized in the transition regime (*28*). In addition, SERS was used to confirm flow-induced polymer conformation changes by examining the redistribution of the π-electron density in the polymer molecule (Fig. 2D and figs. S8 to S10). The most notable change in the spectra is the enhanced intensities of the modes localized in isoindigo units relative to the donor unit for films printed in the transition regime. Because the Raman scattering intensities in conjugated polymers arise from the polarizability of the π-electrons (*29*), this increased peak intensity provides evidence that an increased π-electron density accumulates on the planarized isoindigo ring unit, relative to the donor unit. The change in peak intensity of these Raman modes is accompanied by notable Raman shifts in the range of 3 to 5 cm^{-1} (Fig. 2D). This observation is consistent with the extent and direction of Raman shifts reported in literature when backbone planarization was observed (*30*).

The flow-induced molecular conformation change is accompanied by marked morphological transitions in the PII-2T films across printing regimes. Atomic force microscopy (AFM) phase images and corresponding orientation mapping analysis (*31*) show aligned polymer fibers in the transition regime, in stark contrast to bimodal orientation distributions and twinned domains in the evaporation and LL regimes (Fig. 2E and fig. S11). In the evaporation regime, the "twinned domains" contain fibers oriented approximately 60° and 120° relative to the printing direction, resulting in an average fiber orientation perpendicular to printing (90°). Upon entering the transition regime, the fibers are "straightened out" and reoriented to align with the printing direction (0°). In the LL regime, the fibers return to bimodal orientation distributions because of locally twinned domains. However, unlike in the evaporation regime, the twinned domains do not exhibit long-range ordering. These differences in mesoscale fiber orientation manifest as distinct birefringence characteristics under cross-polarized optical microscopy (CPOM) (Fig. 2, F and G, and fig. S13). We show that the observed flow-induced morphological transition

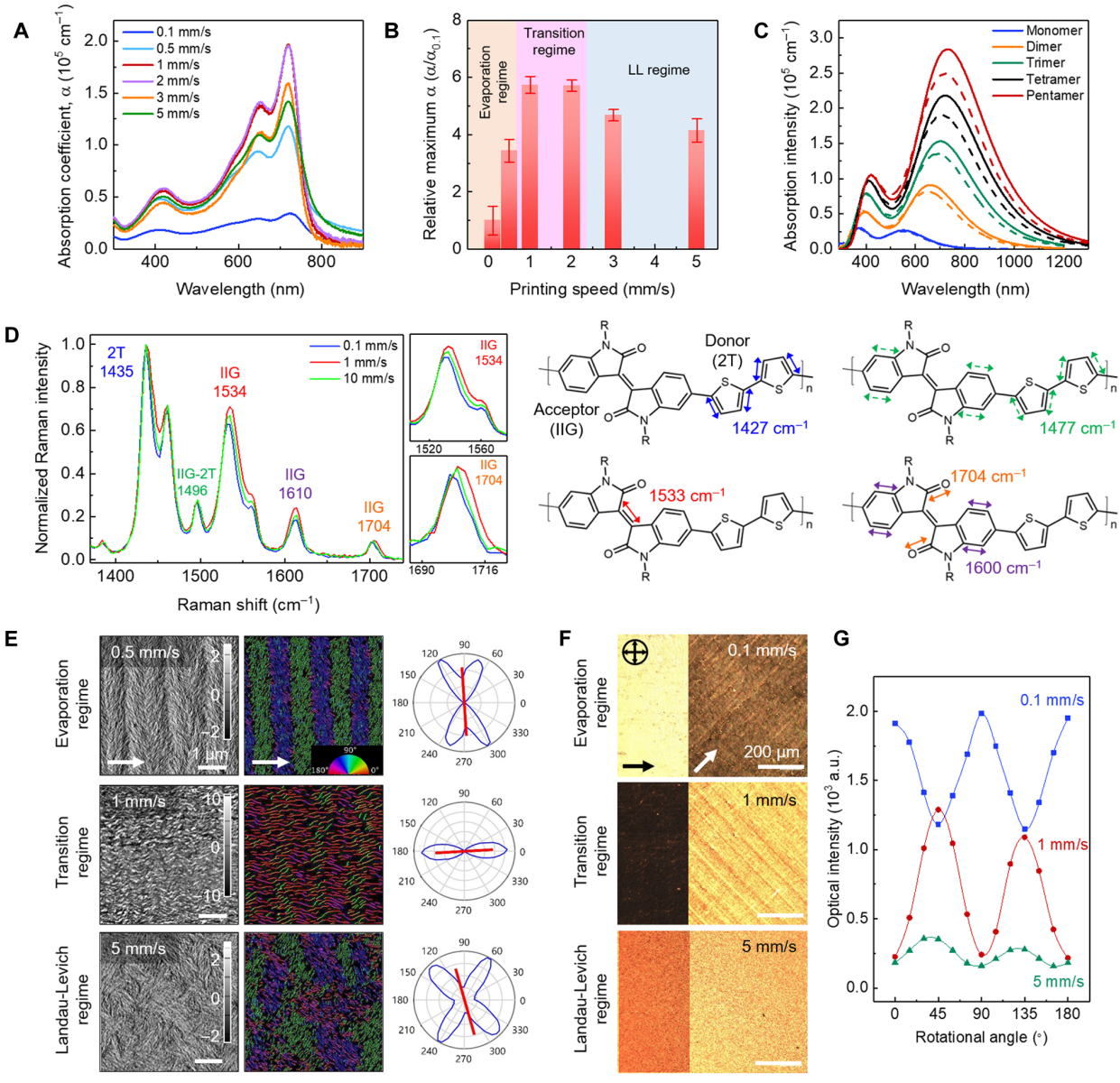

Fig. 2. Flow-induced morphological transition in PII-2T films from molecular, meso- to macroscales. (**A**) Absorption coefficient (α) of the films printed at various printing speeds (0.1 to 5 mm/s). The α values of the PII-2T films are sensitively modulated by the printing speed. The highest α_{max} value of 1.9×10^5 cm^{-1} is obtained in the transition regime (1 mm/s) at 719 nm. (**B**) α_{max} normalized by the α_{max} at 0.1 mm/s as a function of printing speed. All α_{max} values were obtained at ~720 nm corresponding to the 0-0 transition. (**C**) Absorption spectra calculated for oligomers of PII-2T of increasing size at the time-dependent density functional theory (DFT) level [B3LYP functional/6-31 g(d,p) basis set]. Solid and dashed lines denote spectrum of anti- and syn-conformation, respectively. The transition at 733 nm involves highly delocalized hole and electron wave functions along the conjugated backbone. The second absorption band at 403 nm is attributed to the transition localized on the isoindigo units. (**D**) SERS spectra of PII-2T films printed (on a thin gold layer) in the evaporation (0.1 mm/s), transition (1 mm/s), and LL (10 mm/s) regimes (left), with magnified spectra for the 1534 and 1704 cm^{-1} peaks to show the Raman shift (middle). Illustration of representative Raman-active vibrational modes calculated for PII-2T oligomers (right). The peak intensity is normalized by the strongest peak around 1435 cm^{-1}, which is assigned as delocalized C=C stretching over thiophene rings (2T). The peaks around 1534 and 1610 cm^{-1} are assigned as strong localized C=C stretching, and the peak around 1704 cm^{-1} is assigned as C=O stretching in isoindigo units. Solid and dashed arrows indicate the relatively stronger and weaker stretching modes, respectively. (**E**) AFM phase images (left), corresponding orientation mapping analysis (middle), and pole figures of the fibril orientation distribution (right) for the films printed in the evaporation (0.5 mm/s), transition (1 mm/s), and LL (5 mm/s) regimes. The color mapping of fiber orientation ranges from 0° (red), 90° (cyan), to 180° (magenta). The white arrow indicates the printing direction. (**F**) CPOM images of PII-2T films oriented 0° and 45° relative to the polarizer/analyzer for each regime. The arrows indicate the printing direction, and black cross arrows denote cross-polarizers. The exposure time is 80.3 ms for the film printed at 0.1 mm/s and 161 ms for the films printed at 1 and 5 mm/s. (**G**) Optical intensity as a function of relative rotational angle between the printing direction and the polarizer. Note that the exposure time is kept constant (147 ms) for direct comparison of the three cases. The film printed at 0.1 mm/s exhibits higher intensity when the printing direction is oriented parallel (0° and 180°) or perpendicular (90°) to the polarizer, indicating that the polymer backbone is aligned diagonal to the printing direction. In contrast, the film printed at 1 mm/s exhibits higher intensity when the printing direction is oriented at 45° or 135° with respect to the polarizer, indicating the polymer backbone alignment parallel or perpendicular to the printing direction. AFM and GIXD analysis confirmed the former case (shown below). At 5 mm/s, the film still exhibits higher intensity at 45° or 135°, albeit with very low birefringence indicating weak alignment. a.u., arbitrary units.

is insensitive to initial solution concentrations, solvents, substrate surface, and polymer molecular weights (MWs) (figs. S14 to S17). Capillary pen writing was also performed to further demonstrate the generality of our experimental and simulation results, where we again observed similar morphological changes as a result of the evolving flow profile in the meniscus (fig. S18 to S22).

Next, we compare polymer in-plane alignment and out-of-plane orientation distribution across regimes quantified using polarized UV-vis spectroscopy and grazing incidence x-ray diffraction (GIXD). To quantify the extent of polymer alignment, we took UV-vis measurements with the printing direction parallel and perpendicular to the light polarization direction (Fig. 3A and fig. S23) to obtain the dichroic ratio $R_{\text{UV-vis}} = A_{||}/A_{\perp}$. The dichroic ratio shows a notable transition in the polymer backbone orientation between 0.5 and 1 mm/s where the transition regime begins (Fig. 3B). This result is consistent with the switch in optical anisotropy observed using CPOM (Fig. 2F and fig. S13). The highest degree of in-plane alignment indicated by $R_{\text{UV-vis}}$ was reached in the transition regime at 1 mm/s.

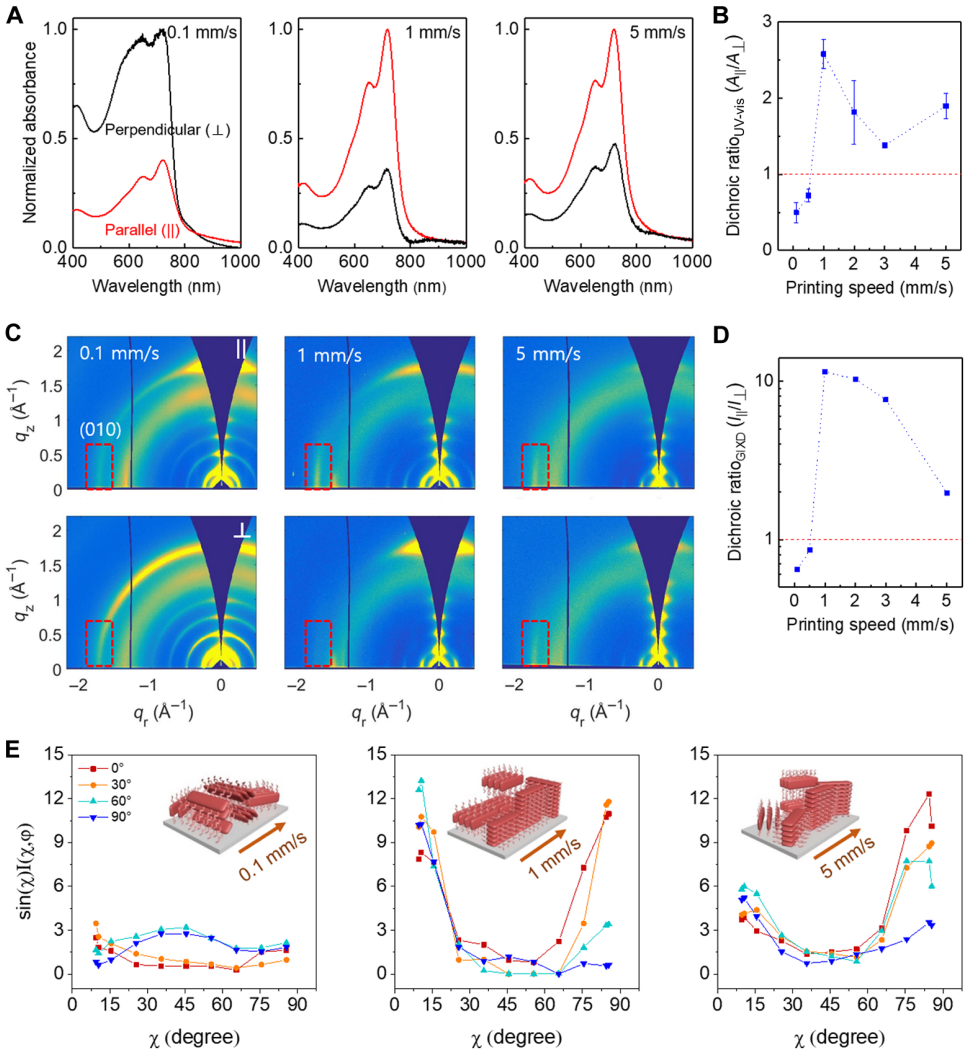

Fig. 3. Flow-induced in-plane alignment and out-of-plane orientation distribution in PII-2T films. (**A**) Normalized absorption spectra of polarized UV-vis spectroscopy with the light polarization direction oriented either parallel (||, red line) or perpendicular (⊥, black line) to the printing direction. The dichroic ratio $R_{\text{UV-vis}}$ ($A_{||}/A_{\perp}$) is 0.40 in the evaporation regime (0.1 mm/s), whereas the $R_{\text{UV-vis}}$ values are 2.82 and 2.12 for the transition (1 mm/s) and LL (5 mm/s) regimes, respectively. (**B**) $R_{\text{UV-vis}}$ plot as a function of printing speed. The $R_{\text{UV-vis}}$ values crossed one from the evaporation to the transition regime, indicating that the polymer backbone is altered from perpendicular to parallel with respect to the printing direction. (**C**) Comparison of 2D x-ray diffraction patterns with the incident beam oriented || and ⊥ to the printing direction. The red dashed boxes mark edge-on π-π stacking (010) peaks. (**D**) R_{GIXD} plot representing an in-plane alignment of edge-on π-stacks as a function of printing speed. High strain rate and low residence time in the transition regime lead to highly aligned polymer aggregates with the backbone parallel to the flow direction. (**E**) Comparison of geometrically corrected intensity of π-π stacking (010) peak as a function of polar angle χ and in-plane rotation angle φ denoting the incident beam directions of φ = 0° (parallel), 30°, 60°, and 90° (perpendicular) with respect to the printing direction. Note that χ = 0° and 90° indicate face-on and edge-on orientation, respectively. Each inset shows the inferred molecular packing structures in PII-2T films printed in three representative regimes. The highest degrees of in-plane and out-of-plane alignment are observed in the transition regime: The backbone is aligned with the printing direction in-plane and adopts a bimodal orientation distribution out-of-plane featuring both edge-on and face-on π-stacks. The rDoC is obtained by integrating the area below each curve. The rDoC is about 480, 835, and 970 for the film produced in the evaporation, transition, and LL regimes, respectively.

We note that the $R_{UV\text{-}vis}$ value can only provide a lower bound on the degree of backbone alignment because the optical transition dipole may have a nonzero component normal to the polymer backbone (*18*). This result was confirmed by GIXD that measures the degree of alignment in the crystalline domains (Fig. 3C and fig. S24). Measurements were performed with the incident beam parallel ($\varphi = 0°$) and perpendicular ($\varphi = 90°$) to the printing direction to obtain the dichroic ratio $R_{GIXD} = I_{||}/I_{\perp}$, where $I_{||}$ and $I_{\perp}$ are the normalized edge-on π-π stacking peak (010) at $\varphi = 0°$ and 90°, respectively. The R_{GIXD} reached as high as 11.4 for the film printed at 1 mm/s, indicating highly aligned crystalline domains, compared to R_{GIXD} of 0.64 and 1.96 for the films printed at 0.1 and 5 mm/s, respectively (Fig. 3D). Further increasing the solution concentration from 10 to 20 mg/ml led to a maximum R_{GIXD} exceeding 50 in the transition regime (fig. S27). Besides in-plane alignment, there are clear differences in the out-of-plane orientation for films printed in each regime, shown in pole figures of the (010) peaks (Fig. 3E). In contrast to broad orientation distributions of π-stacks in films printed at 0.1 or 5 mm/s, a bimodal distribution of both edge-on and face-on π-stacks was observed in the film printed at 1 mm/s. Furthermore, the transition regime not only enhanced alignment in (semi)crystalline domains but also increased the relative degree of crystallinity (rDoC) by ~75% compared to films coated in the evaporation regime. At the same time, paracrystalline disorder as indicated by the g-parameter was reduced from ~13 to ~9% upon entering the transition regime (fig. S24). We attribute the enhanced in-plane and out-of-plane alignment, increased crystallinity, and reduced paracrystalline disorder to backbone planarization in the transition regime. We also observed tilted peaks at $q = \sim 1.42$ Å^{-1} and $\chi = \pm 7 - 15°$ (0.1 mm/s; Fig. 3C) that we attribute to helical aggregates for films produced in the evaporation regime (discussed below). These diffraction features are not present in films coated in the transition and LL regimes as a result of the polymer backbone planarization.

The flow-induced polymer backbone planarization and alignment can enhance charge transport along the polymer backbone and can reduce device cross-talk by imparting charge transport anisotropy. To compare hole mobility and anisotropy across the three regimes, we fabricated bottom-gate top-contact PII-2T field-effect transistors (FETs) containing 24 channels each offset by 15° (see Materials and Methods and Fig. 4A). All electrical characterizations and detailed discussions are summarized in the Supplementary Materials. Figure 4 (B and C) shows the representative drain-source current (I_{DS})–gate-source voltage (V_{GS}) transfer curves and corresponding I_{DS}-V_{DS} output characteristics of the devices, measured with the S-D channels parallel to the printing direction. The transfer curves are nearly ideal, allowing the reliable extraction of hole mobilities (μ_{FET}) in the saturation regime (fig. S29) (*32*). Figure 4D shows charge transport anisotropy characteristics of the films, measured by varying the relative angle (φ) between the S-D channel and the printing direction. As expected, the values of μ_{FET} for the FETs printed at 1 mm/s sensitively depend on φ but much less so for the FETs printed at 0.1 and 5 mm/s. For FETs printed at 1 mm/s, the average μ_{FET} was 1.0 ± 0.13 cm^2 V^{-1} s^{-1} at $\varphi = 0°$, compared to 0.24 ± 0.073 cm^2 V^{-1} s^{-1} at $\varphi = 90°$. This fourfold increase in mobility along the printing direction indicates favorable charge transport along the polymer backbone, which we attribute to reduced torsion angles and high degrees of chain alignment. In contrast, the average mobilities for FETs printed at 0.1 mm/s were μ_{FET} (0°) = 0.35 ± 0.050 and μ_{FET} (90°) = 0.29 ± 0.028 cm^2 V^{-1} s^{-1}. Similar results, μ_{FET} (0°) = 0.32 ± 0.097 and μ_{FET} (90°) = 0.25 ± 0.060 cm^2 V^{-1} s^{-1}, were obtained for FETs printed at 5 mm/s. This isotropic charge transport behavior is consistent with the low degree of orientation ordering in films printed in the evaporation and LL regimes.

We hypothesize that the molecular mechanism underlying the observed morphological transition and electronic property enhancement is the flow-induced backbone planarization in the transition regime. To confirm our hypothesis, we additionally tested several other conjugated polymers by quantum chemical calculations and by analogous experiments (see section S8 for details). First, PTII-2T was adopted as a negative control because its backbone is more planarized when compared to PII-2T due to minimized steric repulsion by thiophene substitution in the isoindigo subunit (*5*). The molecular structures of PII-2T and PTII-2T are shown with their geometry-optimized structures obtained by density functional theory calculation (Fig. 5, A and B). Notably, the systematic torsion within each repeat unit of PII-2T causes its backbone to adopt a slight twist conformation, whereas PTII-2T forms a relatively high coplanar backbone (fig. S31). Two diketopyrrolopyrrole (DPP)–based polymers, DPP-BTz and DPP2T-TT, were also chosen as extended examples of D-A–conjugated copolymer systems. We infer that DPP-BTz exhibits backbone torsion whereas DPP2T-TT is more planar, as compared with the UV-vis absorption spectra of DPP-BTz and DPP2T-TT (fig. S33). The 0-0 electronic transition of DPP-BTz films (~870 nm) is considerably red shifted than the solution sample (838 nm) whereas the difference is negligible between DPP2T-TT films and solution (~815 nm).

Having chosen two pairs of twisted D-A polymers and their planar counterparts, we investigate their conformation change across the printing regimes by comparing the α_{max} of the printed polymer films (Fig. 5, C to J). In the evaporation regime, the α_{max} values ($\sim 5.0 \times 10^4$ cm^{-1}) of PII-2T and DPP-BTz are about three times lower than those of PTII-2T and DPP2T-TT ($\sim 1.5 \times 10^5$ cm^{-1}). This weaker energy absorption for PII-2T or DPP-BTz can be understood to arise from a particularly strong localization of the lowest unoccupied molecular orbital and/or a strong interunit torsion. In addition, the α_{max} values change across printing regimes is drastic for DPP-BTz, and the highest α_{max} values is again attained in the transition regime (Fig. 5, E and I). This is consistent with the results of PII-2T (Fig. 5, C and G) and can be attributed to the polymer backbone planarization under high strain rate and low residence time in the transition regime. In contrast, the absorption bands of PTII-2T and DPP2T-TT show little variation in intensity across regimes (Fig. 5, D, F, H, and J) likely because they already adopt a planarized conformation and are thus less influenced by the flow. The morphological transitions of the four polymer films show consistent correlation with flow-induced molecular conformation change (Fig. 5K and fig. S34). Twinned domains diminished for PII-2T and DPP-BTz when no transition is observed for PTII-2T and DPP2T-TT. We also show a similar morphological transition when using low-MW PII-2T to confirm that this flow-induced transition is independent of MW (see figs. S16 and S17). Only in the cases of flow-induced backbone planarization and morphological transition did we observe enhanced alignment in films printed in the transition regime (fig. S35).

We lastly connect the molecular mechanism with the macroscale morphological transition to show that flow alters the polymer assembly pathways by eliminating a chiral, intermediate mesophase upon planarizing the polymer backbone. For all four polymer systems, we performed in situ CPOM imaging of solution- to solid-state phase transition in a receding meniscus driven by solvent evaporation. The range of meniscus receding speeds falls under the evaporation regime. We observed the appearance of a lyotropic liquid crystalline

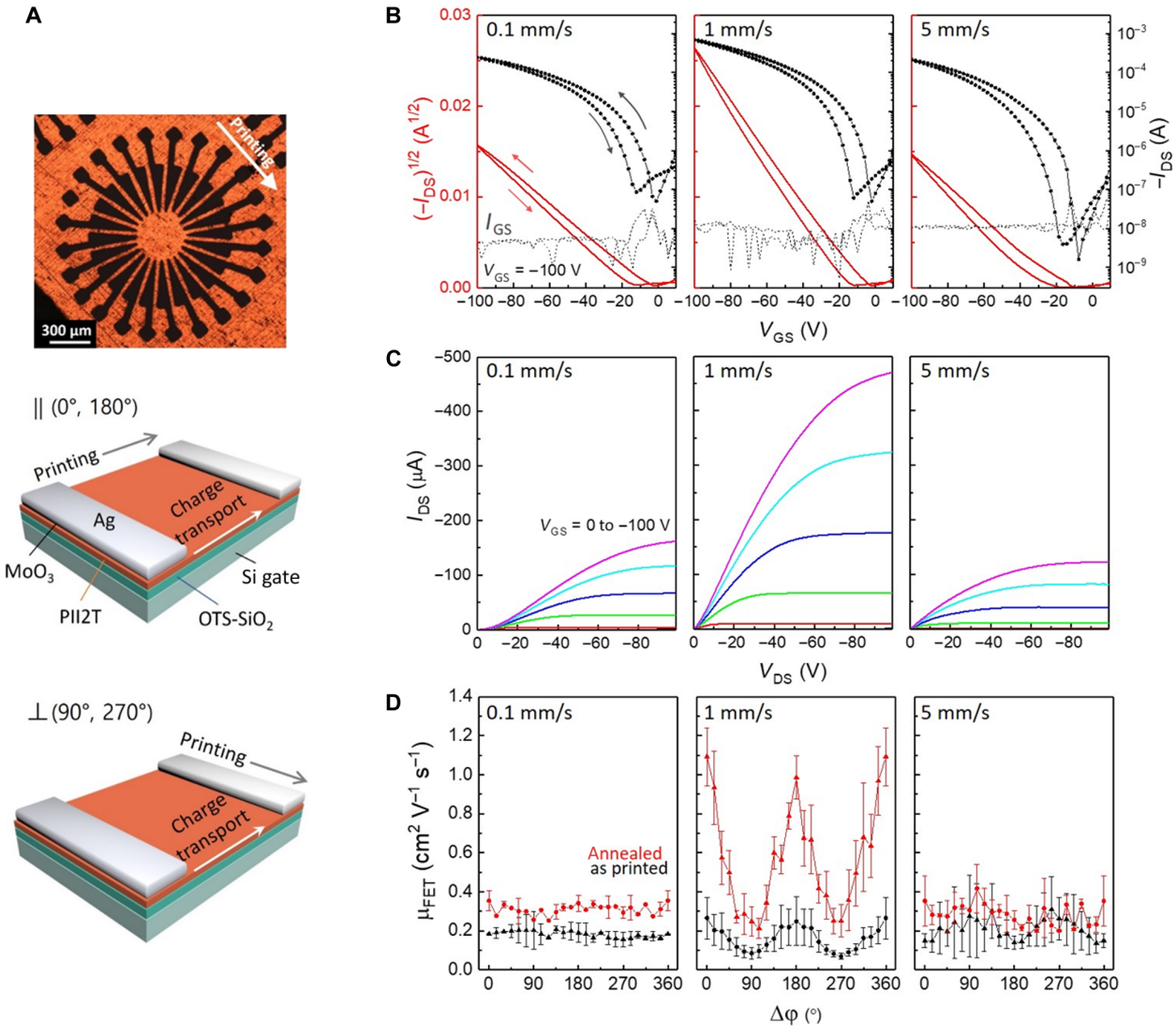

Fig. 4. PII-2T FET device performance and charge transport anisotropy. (**A**) CPOM image of a set of circularly configured FETs. An array of silver electrodes (black) are deposited on the PII-2T film (orange) to form bottom-gate top-contact FET channels separated by 15°. The channel length (L) and width (W) are 26 and 360 μm, respectively. The charge transport anisotropy of the films can be precisely determined by the relative angle (φ) of S-D locations with respect to the printing direction. Schematic of the device geometry showing typical parallel (φ = 0° or 180°) or perpendicular (φ = 90° or 270°) device measurement. (**B**) Double-sweep transfer characteristics of PII-2T FET devices in log scale of drain current (black line with dots) and linear scale of the square root of the drain current (red line) at V_{DS} = −100 V. The arrows indicate the direction of the V_{GS} sweep. The dotted gray lines show the gate leakage current I_{GS}, which is consistently low. The electrical parameters calculated for the PII-2T FET printed at 0.1 mm/s are a field-effect mobility (μ_{FET}) of 0.39 $cm^2 V^{-1} s^{-1}$, a threshold voltage (V_{TH}) of −6.6 V, and an on/off current ratio (I_{ON}/I_{OFF}) of 4.9×10^3. The FET printed at 1 mm/s resulted in a μ_{FET} of 1.1 $cm^2 V^{-1} s^{-1}$, a V_{TH} of −9.3 V, and an I_{ON}/I_{OFF} of 1.3×10^4. The FET printed at 5 mm/s yielded a μ_{FET} of 0.41 $cm^2 V^{-1} s^{-1}$, a V_{TH} of −18 V, and an I_{ON}/I_{OFF} of 1.3×10^5. Notably, these results correspond to annealed devices at 200°C to enhance crystallinity and to improve charge transport (fig. S30). (**C**) Corresponding output characteristics of FET devices. Notably, the contact resistance (inferred from the shape of the output curve near origin) is prominently reduced on the films printed at 1 and 5 mm/s when compared to that of film printed at 0.1 mm/s because of the decreased surface roughness and film thickness. (**D**) Hole mobility of FET devices as a function of φ. High charge transport anisotropy is observed for films produced in the transition regime because of a high degree of backbone alignment. The extent of charge transport anisotropy is enhanced through thermal annealing.

mesophase preceding the dried thin film for the torsional PII-2T and DPP-BTz but not for the more planar PTII-2T and DPP2T-TT (Fig. 6, A to D, and movies S1 to S4). The mesophase exhibited a rope-like texture that was carried over into the film domain. This suggests that the twinned morphologies observed for PII-2T and DPP-BTz (absent from PTII-2T and DPP2T-TT) are a result of their intermediate mesophase. We hypothesize that the observed mesophase is a twist-bend nematic (N_{TB}) phase, which can form from twisted or bent achiral molecules upon assembly into helical aggregates (*33*, *34*). The helical aggregates then form chiral twinned domains with a helical pitch on the scale of several nanometers to micrometers (*35*, *36*). Although an N_{TB} phase has not been reported for conjugated polymers, it has been postulated that polymers with a gross bent structure are likely to exhibit N_{TB} phase (*34*). We provide direct evidence that PII-2T exhibits a lyotropic, chiral mesophase upon increasing solution concentration (fig. S36). We also observed signatures of helical aggregates in GIXD patterns

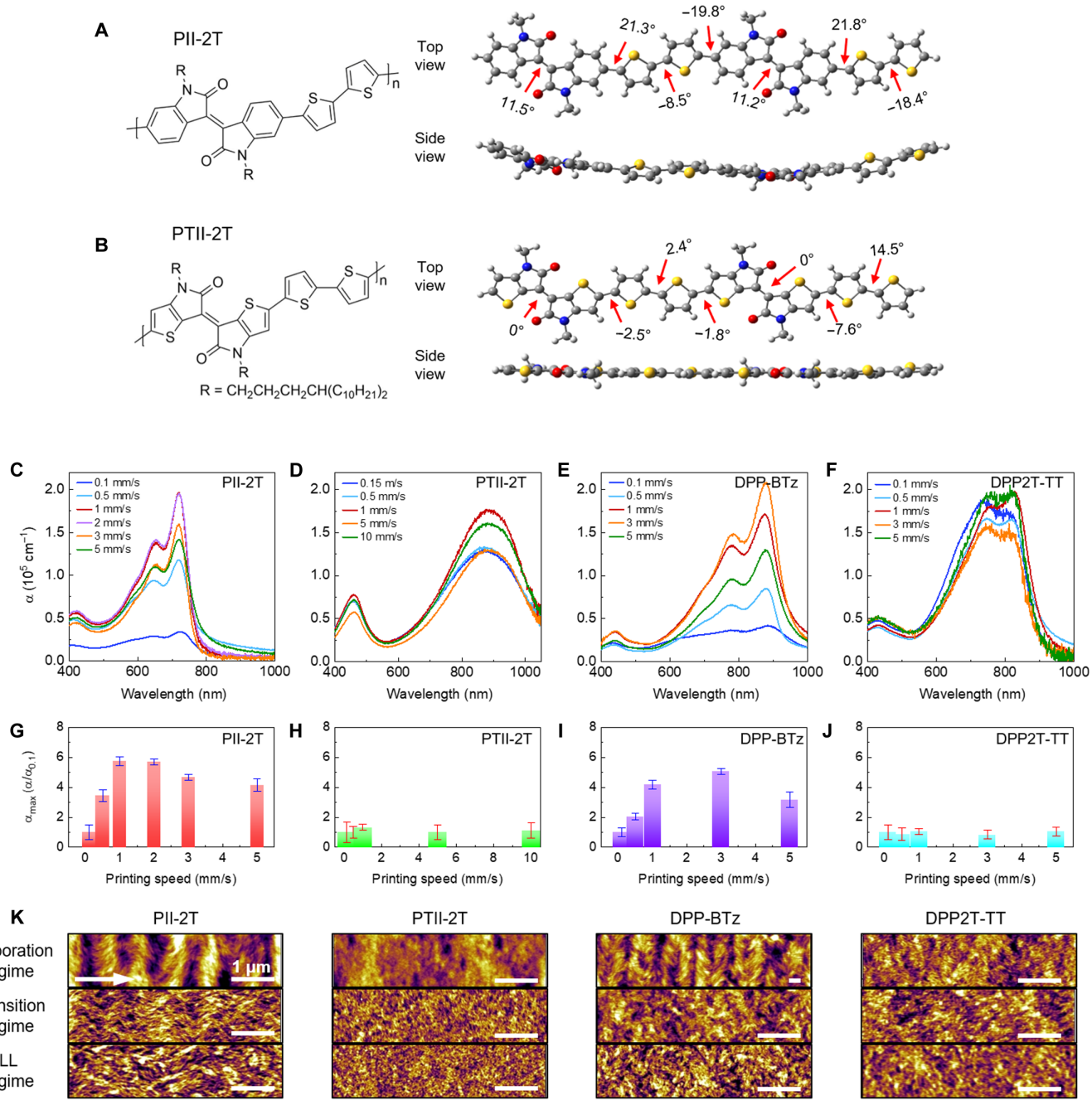

Fig. 5. Molecular structure–dependent flow-induced morphological transition of polymers. (**A** and **B**) Molecular structures of PII-2T (A) and PTII-2T (B), and corresponding optimized dimers with average torsional angles based on DFT calculations at the B3LYP/6-31 g(d,p) level. Side view of energy-minimized conformers depicts the varying degrees of backbone coplanarity. The systematic torsion within each repeat unit of PII-2T causes its backbone to adopt a slight twist conformation, whereas the backbone of PTII-2T yields relatively high coplanar chains. (**C** to **F**) Absorption spectra of PII-2T (C), PTII-2T (D), DPP-BTz (E), and DPP2T-TT (F) polymer films as a function of printing speed. The α_{max} values obtained for the lowest speed are 3.4×10^4 (PII-2T), 1.2×10^5 (PTII-2T), 4.1×10^4 (DPP-BTz), and 1.8×10^5 cm^{-1} (DPP2T-TT). (**G** to **J**) α_{max} normalized by the lowest α_{max} for PII-2T (G), PTII-2T (H), DPP-BTz (I), and DPP2T-TT (J) polymer system. The α_{max} varies largely with printing speeds for PII-2T and DPP-BTz, showing the highest values for the films produced in the transition regime. In contrast, PTII-2T and DPP2T-TT are less influenced by flow. (**K**) AFM height images of the polymer films for the three regimes. The white arrow indicates the printing direction. Scale bars, 1 μm. Flow-induced morphological transition is observed for PII-2T and DPP-BTz, in which the twinned domains are diminished upon entering the transition regime.

of PII-2T, which are tilted peaks at q = ~1.42 $Å^{-1}$ and $\chi = \pm 7 - 15°$ for films produced in the evaporation regime (Fig. 3C). We note that these peaks appear at a tilted angle shown in the I-χ plot (fig. S37). We propose that these tilted peaks arise from intermolecular stacking within the helical aggregates formed by twisted polymer chains. This is also supported by the fact that these tilted peaks are only seen for films printed in the evaporation regime and are absent for films printed in the transition and LL regimes. Similar GIXD results have

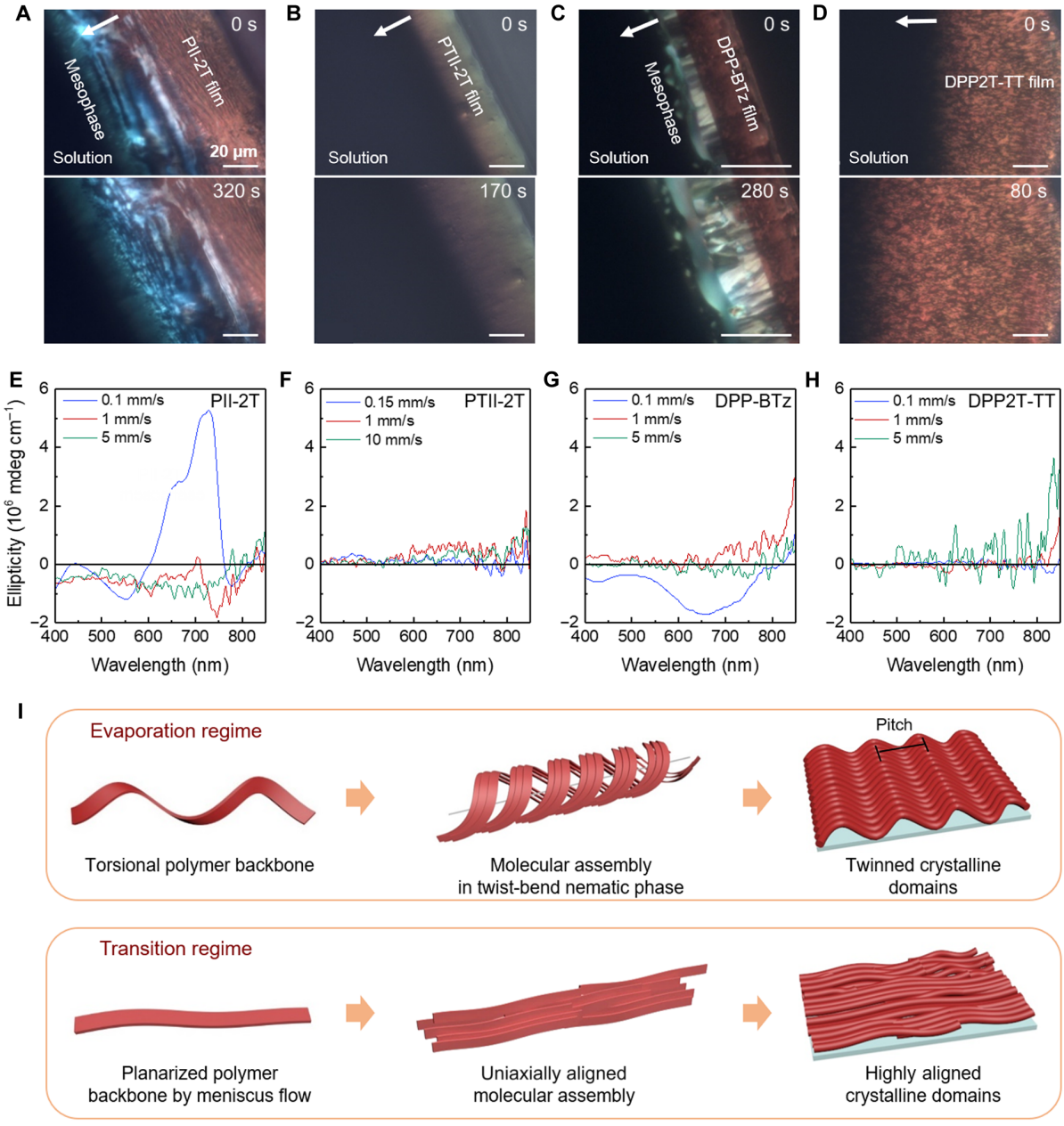

Fig. 6. Flow-controlled polymer assembly mechanism. (**A** to **D**) CPOM images of PII-2T (A), PTII-2T (B), DPP-BTz (C), and DPP2T-TT (D) solution- to solid-state phase transition in a receding meniscus driven by solvent evaporation. Note that the meniscus receding speeds are approximately 0.01 to 0.05 mm/s, corresponding to evaporation regime. The white arrows indicate the meniscus receding direction. Notably, PII-2T and DPP-BTz exhibit strong birefringence near the contact line, indicating crystalline mesophase formation. In contrast, no such mesophase is observed for PTII-2T and DPP2T-TT. (**E** to **H**) CD spectra of PII-2T (E), PTII-2T (F), DPP-BTz (G), and DPP2T-TT (H) polymer films as a function of printing speed. Each low, intermediate, and fast speed corresponds to the evaporation, transition, and LL regime, respectively. Only PII-2T and DPP-BTz films printed in the evaporation regime exhibit CD signals, corroborating the formation of chiral, twinned domains mediated by a twist-bend nematic phase (A and C). In contrast, PTII-2T and DPP2T-TT do not show substantial CD signals, corresponding to the absence of an intermediate twist-bend nematic phase (B and D). (**I**) Schematic illustration of the inferred flow-controlled polymer assembly mechanism. In the evaporation regime, torsional polymer molecules assemble in a helical fashion to form an N_{TB} mesophase. The helical polymer fibers subsequently assemble into the twinned domains. The chirality in twinned morphology is caused by the helicity of the N_{TB} phase. Given the higher strain in the transition regime, the twisted molecule is stretched out/planarized to eliminate the N_{TB} mesophase, resulting in uniaxially aligned morphology.

been reported for bent mesogenic molecules self-assembled into helical nanofilaments in nanopores (*37*).

We further confirmed the formation of chiral twinned domains in PII-2T and DPP-BTz thin films, characteristic of the preceding N_{TB} phase, via CPOM and circular dichroism (CD) spectroscopy. By rotating the thin films under fixed crossed polarizers, we observed alternating dark and bright band patterns characteristic of twinned domains (figs. S38 and S39) (*38*, *39*). Furthermore, CD spectra of the

PII-2T and DPP-BTz twinned films showed strong CD signals indicating chirality, which was not observed from PTII-2T and DPP2T-TT films (Fig. 6, E to H, and fig. S40). The CD response of PII-2T and DPP-BTz almost vanished for the films printed in the transition and LL regimes probably because of the flow-induced backbone planarization that eliminated the N_{TB} mesophase and thus diminished the chirality of the films to lead to highly aligned domain morphology. The proposed mechanism of hierarchical assembly and morphological transition is illustrated in Fig. 6I.

CONCLUSIONS

In summary, we first report printing flow–directed assembly as a general nonsynthetic approach for tuning torsional angles between successive building blocks of conjugated polymers and the resultant electronic properties. Upon twisted-to-planar polymer conformation change, the twist-bend liquid crystalline phase is eliminated to result in highly aligned printed polymer thin films. Because of the substantially increased conjugation length and degree of alignment upon backbone planarization, enhanced charge carrier mobility and charge transport anisotropy are obtained for corresponding FET devices. While molecular design and synthesis are the dominant approach for tuning equilibrium conformation, thin film morphology, and electronic structures, rational design of printing flow can provide an alternative approach that is simple yet highly effective for controlling multiscale assembly and enhancing charge transport for a diverse range of conjugated polymers. Because fluid flow is ubiquitous in all solution processing techniques, we expect that flow design will be an integral part of morphological control for high-performance organic electronics. Furthermore, our mechanistic insights on flow-directed assembly can inspire the morphology control of functional materials beyond printed electronics.

MATERIALS AND METHODS

Materials

The isoindigo-based copolymers such as high-MW PII-2T [number-average MW (M_n) = 230,174 g/mol, weight-average MW (M_w) = 715,643 g/mol, and polydispersity index (PDI) = 3.1], low-MW PII-2T (M_n = 117,635 g/mol, M_w = 291,735 g/mol, and PDI = 2.4), and PTII-2T (the MW could not be measured because of its strong interaction with the column material even in high-temperature gas permeation chromatography measurement) were synthesized as previously described (*40*, *41*). The DPP-based polymers such as DPP-BTz (M_n = 121,185 g/mol, M_w = 285,632 g/mol, and PDI = 2.3) and DPP2T-TT (M_n = 60,732 g/mol, M_w = 195,723 g/mol, and PDI = 3.2) were synthesized following a previously published procedure (*22*, *23*). The solution was prepared by dissolving the polymer (1 to 30 mg/ml) in chloroform (99.8%; Sigma-Aldrich Inc.) or 1,2-dichlorobenzene (o-DCB; anhydrous, 99%; Sigma-Aldrich Inc.). A heavily doped n-type Si with a 300-nm-thick, thermally grown SiO_2 layer was used as an oxide substrate. Corning glass substrates were used for spectroscopic studies. The substrates were cleaned with toluene, acetone, and isopropyl alcohol and then blow-dried with a stream of nitrogen to remove contaminants. The surfaces of all substrates were modified by a hydrophobic self-assembled monolayer (SAM) treatment. The SAM treatment was achieved by immersing the plasma-activated substrates in a dilute solution (0.1 volume %) of *n*-octyldecyltrichlorosilane (OTS; 95%; Acros) with trichloroethylene (anhydrous, >99.5%; Sigma-Aldrich Inc.) at room temperature for 20 min. The treated substrates were then rinsed with toluene, dried with nitrogen, and annealed at 120°C for 20 min.

MGP of conjugated polymer films

PII-2T films were printed onto substrates by an MGP method such as blade coating or capillary pen writing. The blade coating method was reported in our previous publications (*20*). Briefly, an OTS-treated Si substrate was used as a blade set at an angle of 7°, with a gap of 100 μm between the substrate and the blade. The blade was linearly translated over the stationary substrate while retaining the ink solution within the gap. The PII-2T, DPP-BTz, and DPP2T-TT films were prepared on OTS-treated SiO_2/glass substrates at printing speeds ranging from 0.1 to 5 mm/s with a substrate temperature of 25°C. Only PTII-2T films were printed on bare SiO_2/glass substrates at printing speeds ranging from 0.15 to 10 mm/s at the same temperature because stick and slip phenomena was too dominant on hydrophobic surfaces. The standard concentration of all polymer solutions was 10 mg/ml dissolved in chloroform. A PII-2T/o-DCB solution (30 mg/ml) was also used to deposit polymer films on OTS-treated SiO_2 substrates, at printing speeds ranging from 0.05 to 0.25 mm/s with a substrate temperature of 60°C.

For capillary pen writing, a capillary pen was obtained from a commercially available water-based pen (Plus Pen 3000, Monami) as previously reported for patterning organic semiconductors (*21*). The commercial ink from the pen was completely removed by applying washing cycles involving sonication with ethanol and water, drying with nitrogen, and annealing at 60°C overnight. The capillary pen was then mounted vertically on our printing system. The polymer ink solution was supplied to the pen by capillary action from the top of the pen using a micropipette. The ink solution was then drawn from the bottom of the pen when the nib touched the substrate surface. The pen was slightly raised while maintaining the ink solution meniscus so that the average gap between the pen tip and substrate was approximately 10 μm. The PII-2T films were printed using a PII-2T/o-DCB solution (30 mg/ml) on OTS-treated SiO_2 substrates, at printing speeds ranging from 0.05 to 5 mm/s with a substrate temperature of 60°C.

Characterization techniques

The birefringence of polymer films was observed using CPOM (Eclipse Ci-POL, Nikon). The mesoscale morphology and film thickness were characterized using tapping mode AFM (Asylum Research Cypher). UV-vis (Cary 60 UV-Vis, Agilent) spectroscopy was used to calculate the absorption coefficient of films and investigate polymer alignment using polarized UV-vis. GIXD measurements were performed at beamline 8-ID-E at the Argonne National Laboratory, with an incident beam energy of 7.35 keV on a 2D detector (PILATUS 1M) at a 208-mm sample-to-detector distance. Samples were scanned for 10 s in a helium chamber. We performed surface (film-air interface) and bulk GIXD to probe the morphology through the depth of the films. The x-ray incident angle was set to be above (0.14°) and below (0.04°) the critical angle (≈0.1°) of the organic layer to probe the molecular packing throughout the entire film and near the top surface layer (penetration depth, approximately 5 nm), respectively. The samples were scanned with the incident beam parallel and perpendicular to the printing direction by rotating the substrate. The molecular conformation was analyzed using a Raman confocal imaging microscope (LabRAM HR 3D-capable Raman spectroscopy imaging system, Horiba) with ×100 objective lens equipped with a Horiba Synapse

back-illuminated deep-depletion charge-coupled device camera. A 532-nm laser (maximum power, 50 mW; Laser Quantum) was used as the excitation source. Integration times of 10 s were used for each measurement. An optical density (OD) filter = 1 was used [OD = log (power transmission factor)] after confirming that there was no beam damage to the sample. All electrical measurements were performed in a nitrogen environment using a Keysight B1500A semiconductor parameter analyzer. CD spectra were recorded using a JASCO J-810 spectrophotometer.

SUPPLEMENTARY MATERIALS

Supplementary material for this article is available at http://advances.sciencemag.org/cgi/content/full/5/8/eaaw7757/DC1

REFERENCES AND NOTES

1. A. Facchetti, π-conjugated polymers for organic electronics and photovoltaic cell applications. *Chem. Mater.* **23**, 733–758 (2011).
2. H. Y. Wang, Y. Xu, X. Yu, R. Xing, J. Liu, H. Yanchun, Structure and morphology control in thin films of conjugated polymers for an improved charge transport. *Polymers* **5**, 1272–1324 (2013).
3. D. Venkateshvaran, M. Nikolka, A. Sadhanala, V. Lemaur, M. Zelazny, M. Kepa, M. Hurhangee, A. J. Kronemeijer, V. Pecunia, I. Nasrallah, I. Romanov, K. Broch, I. McCulloch, D. Emin, Y. Olivier, J. Cornil, D. Beljonne, H. Sirringhaus, Approaching disorder-free transport in high-mobility conjugated polymers. *Nature* **515**, 384–388 (2014).
4. X. Zhang, H. Bronstein, A. J. Kronemeijer, J. Smith, Y. Kim, R. J. Kline, L. J. Richter, T. D. Anthopoulos, H. Sirringhaus, K. Song, M. Heeney, W. Zhang, I. McCulloch, D. M. DeLongchamp, Molecular origin of high field-effect mobility in an indacenodithiophene–benzothiadiazole copolymer. *Nat. Commun.* **4**, 2238 (2013).
5. M. S. Chen, J. R. Niskala, D. A. Unruh, C. K. Chu, O. P. Lee, J. M. J. Fréchet, Control of polymer-packing orientation in thin films through synthetic tailoring of backbone coplanarity. *Chem. Mater.* **25**, 4088–4096 (2013).
6. J. Lee, H. Ko, E. Song, H. G. Kim, K. Cho, Naphthodithiophene-based conjugated polymer with linear, planar backbone conformation and strong intermolecular packing for efficient organic solar cells. *ACS Appl. Mater. Interfaces* **7**, 21159–21169 (2015).
7. C. Z. Zhu, L. Fang, Locking the coplanar conformation of π-conjugated molecules and macromolecules using dynamic noncovalent bonds. *Macromol. Rapid Commun.* **39**, 1700241 (2018).
8. H. Huang, L. Yang, A. Facchetti, T. J. Marks, Organic and polymeric semiconductors enhanced by noncovalent conformational locks. *Chem. Rev.* **117**, 10291–10318 (2017).
9. D. Kajiya, S. Ozawa, T. Koganezawa, K.-i. Saitow, Enhancement of out-of-plane mobility in P3HT film by rubbing: Aggregation and planarity enhanced with low regioregularity. *J. Phys. Chem. C* **119**, 7987–7995 (2015).
10. J. P. Schmidtke, J.-S. Kim, J. Gierschner, C. Silva, R. H. Friend, Optical spectroscopy of a polyfluorene copolymer at high pressure: Intra- and intermolecular interactions. *Phys. Rev. Lett.* **99**, 167401 (2007).
11. A. J. Pennings, V. Jm, A. M. Kiel, Hydrodynamically induced crystallization of polymers from solution. *Kolloid Z. Z. Polym.* **237**, 336–358 (1970).
12. A. Keller, H. W. H. Kolnaar, Flow-induced orientation and structure formation, in *Materials Science and Technology* (Wiley-VCH Verlag GmbH & Co. KGaA, 2006).
13. G. Lamberti, Flow induced crystallisation of polymers. *Chem. Soc. Rev.* **43**, 2240–2252 (2014).
14. Z. Wang, Z. Ma, L. B. Li, Flow-induced crystallization of polymers: Molecular and thermodynamic considerations. *Macromolecules* **49**, 1505–1517 (2016).
15. G. Giri, E. Verploegen, S. C. B. Mannsfeld, S. Atahan-Evrenk, D. H. Kim, S. Y. Lee, H. A. Becerril, A. Aspuru-Guzik, M. F. Toney, Z. Bao, Tuning charge transport in solution-sheared organic semiconductors using lattice strain. *Nature* **480**, 504–508 (2011).
16. Y. Diao, B. C.-K. Tee, G. Giri, J. Xu, D. H. Kim, H. A. Becerril, R. M. Stoltenberg, T. H. Lee, G. Xue, S. C. B. Mannsfeld, Z. Bao, Solution coating of large-area organic semiconductor thin films with aligned single-crystalline domains. *Nat. Mater.* **12**, 665–671 (2013).

17. Y. Diao, Y. Zhou, T. Kurosawa, L. Shaw, C. Wang, S. Park, Y. Guo, J. A. Reinspach, K. Gu, X. Gu, B. C. K. Tee, C. Pang, H. Yan, D. Zhao, M. F. Toney, S. C. B. Mannsfeld, Z. Bao, Flow-enhanced solution printing of all-polymer solar cells. *Nat. Commun.* **6**, 7955 (2015).
18. S. Schott, E. Gann, L. Thomsen, S.-H. Jung, J.-K. Lee, C. R. McNeill, H. Sirringhaus, Charge-transport anisotropy in a uniaxially aligned diketopyrrolopyrrole-based copolymer. *Adv. Mater.* **27**, 7356–7364 (2015).
19. G. Wang, W. Huang, N. D. Eastham, S. Fabiano, E. F. Manley, L. Zeng, B. Wang, X. Zhang, Z. Chen, R. Li, R. P. H. Chang, L. X. Chen, M. J. Bedzyk, F. S. Melkonyan, A. Facchetti, T. J. Marks, Aggregation control in natural brush-printed conjugated polymer films and implications for enhancing charge transport. *Proc. Natl. Acad. Sci. U.S.A.* **114**, E10066–E10073 (2017).
20. E. Mohammadi, C. Zhao, Y. Meng, G. Qu, F. Zhang, X. Zhao, J. Mei, J.-M. Zuo, D. Shukla, Y. Diao, Dynamic-template-directed multiscale assembly for large-area coating of highly-aligned conjugated polymer thin films. *Nat. Commun.* **8**, 16070 (2017).
21. B. Kang, H. Min, U. Seo, J. Lee, N. Park, K. Cho, H. S. Lee, Directly drawn organic transistors by capillary pen: A new facile patterning method using capillary action for soluble organic materials. *Adv. Mater.* **25**, 4117–4122 (2013).
22. M. Gruber, S.-H. Jung, S. Schott, D. Venkateshvaran, A. J. Kronemeijer, J. W. Andreasen, C. R. McNeill, W. W. H. Wong, M. Shahid, M. Heeney, J.-K. Lee, H. Sirringhaus, Enabling high-mobility, ambipolar charge-transport in a DPP-benzotriazole copolymer by side-chain engineering. *Chem. Sci.* **6**, 6949–6960 (2015).
23. Z. Chen, M. J. Lee, R. S. Ashraf, Y. Gu, S. Albert-Seifried, M. M. Nielsen, B. Schroeder, T. D. Anthopoulos, M. Heeney, I. McCulloch, H. Sirringhaus, High-performance ambipolar diketopyrrolopyrrole-thieno[3,2-*b*]thiophene copolymer field-effect transistors with balanced hole and electron mobilities. *Adv. Mater.* **24**, 647–652 (2012).
24. G. Qu, J. J. Kwok, Y. Diao, Flow-directed crystallization for printed electronics. *Acc. Chem. Res.* **49**, 2756–2764 (2016).
25. M. Le Berre, Y. Chen, D. Baigl, From convective assembly to Landau-Levich deposition of multilayered phospholipid films of controlled thickness. *Langmuir* **25**, 2554–2557 (2009).
26. M. S. Vezie, S. Few, I. Meager, G. Pieridou, B. Dörling, R. S. Ashraf, A. R. Goñi, H. Bronstein, I. McCulloch, S. C. Hayes, M. Campoy-Quiles, J. Nelson, Exploring the origin of high optical absorption in conjugated polymers. *Nat. Mater.* **15**, 746–753 (2016).
27. N. J. Hestand, F. C. Spano, The effect of chain bending on the photophysical properties of conjugated polymers. *J. Phys. Chem. B* **118**, 8352–8363 (2014).
28. M. Marcus, O. R. Tozer, W. Barford, Theory of optical transitions in conjugated polymers. II. Real systems. *J. Chem. Phys.* **141**, 164102 (2014).
29. S. Wood, J.-H. Kim, J. Wade, J. B. Park, D.-H. Hwang, J.-S. Kim, Systematic control of heteroatoms in donor–acceptor copolymers and its effects on molecular conformation and photovoltaic performance. *J. Mater. Chem. C* **4**, 7966–7978 (2016).
30. S. Sweetnam, K. Vandewal, E. Cho, C. Risko, V. Coropceanu, A. Salleo, J.-L. Brédas, M. D. McGehee, Characterizing the polymer:Fullerene intermolecular interactions. *Chem. Mater.* **28**, 1446–1452 (2016).
31. N. E. Persson, M. A. McBride, M. A. Grover, E. Reichmanis, Automated analysis of orientational order in images of fibrillar materials. *Chem. Mater.* **29**, 3–14 (2016).
32. H. H. Choi, K. Cho, C. D. Frisbie, H. Sirringhaus, V. Podzorov, Critical assessment of charge mobility extraction in FETs. *Nat. Mater.* **17**, 2–7 (2018).
33. I. Dozov, On the spontaneous symmetry breaking in the mesophases of achiral banana-shaped molecules. *Europhys. Lett.* **56**, 247–253 (2001).
34. R. J. Mandle, J. W. Goodby, Progression from nano to macro science in soft matter systems: Dimers to trimers and oligomers in twist-bend liquid crystals. *RSC Adv.* **6**, 34885–34893 (2016).
35. D. Chen, J. H. Porada, J. B. Hooper, A. Klittnick, Y. Shen, M. R. Tuchband, E. Korblova, D. Bedrov, D. M. Walba, M. A. Glaser, J. E. Maclennan, N. A. Clark, Chiral heliconical ground state of nanoscale pitch in a nematic liquid crystal of achiral molecular dimers. *Proc. Natl. Acad. Sci. U.S.A.* **110**, 15931–15936 (2013).
36. D. A. Paterson, M. Gao, Y.-K. Kim, A. Jamali, K. L. Finley, B. Robles-Hernández, S. Diez-Berart, J. Salud, M. R. de la Fuente, B. A. Timimi, H. Zimmermann, C. Greco, A. Ferrarini, J. M. D. Storey, D. O. López, O. D. Lavrentovich, G. R. Luckhurst, C. T. Imrie, Understanding the twist-bend nematic phase: The characterisation of 1-(4-cyanobiphenyl-4'-yloxy)-6-(4-cyanobiphenyl-4'-yl)hexane (CB6OCB) and comparison with CB7CB. *Soft Matter* **12**, 6827–6840 (2016).
37. H. Kim, S. Lee, T. J. Shin, E. Korblova, D. M. Walba, N. A. Clark, S. B. Lee, D. K. Yoon, Multistep hierarchical self-assembly of chiral nanopore arrays. *Proc. Natl. Acad. Sci. U.S.A.* **111**, 14342–14347 (2014).
38. W.-J. Chung, J.-W. Oh, K. Kwak, B. Y. Lee, J. Meyer, E. Wang, A. Hexemer, S.-W. Lee, Biomimetic self-templating supramolecular structures. *Nature* **478**, 364–368 (2011).
39. Y. Yang, H. Pei, G. Chen, K. T. Webb, L. J. Martinez-Miranda, I. K. Lloyd, Z. Lu, K. Liu, Z. Nie, Phase behaviors of colloidal analogs of bent-core liquid crystals. *Sci. Adv.* **4**, eaas8829 (2018).
40. T. Lei, J.-H. Dou, J. Pei, Influence of alkyl chain branching positions on the hole mobilities of polymer thin-film transistors. *Adv. Mater.* **24**, 6457–6461 (2012).
41. G. W. P. Van Pruissen, F. Gholamrezaie, M. M. Wienk, R. A. J. Janssen, Synthesis and properties of small band gap thienoisoindigo based conjugated polymers. *J. Mater. Chem.* **22**, 20387–20393 (2012).
42. F. Doumenc, B. Guerrier, Drying of a solution in a meniscus: A model coupling the liquid and the gas phases. *Langmuir* **26**, 13959–13967 (2010).
43. J. Plawsky, A. Chatterjee, P. C. Wayne Jr., Modeling contact line dynamics in evaporating menisci, in *Proceedings of the Comsol User's Conference* (2009).
44. J. A. Emerson, D. T. W. Toolan, J. R. Howse, E. M. Furst, T. H. Epps, Determination of solvent–polymer and polymer–polymer Flory–Huggins interaction parameters for poly(3-hexylthiophene) via solvent vapor swelling. *Macromolecules* **46**, 6533–6540 (2013).
45. M. M. Tirado, C. L. Martínez, J. G. de la torre, Comparison of theories for the translational and rotational diffusion coefficients of rod-like macromolecules. Application to short DNA fragments. *J. Chem. Phys.* **81**, 2047–2052 (1984).
46. J. Xu, Y. Diao, D. Zhou, Y. Mao, G. Giri, W. Chen, N. Liu, S. C. B. Mannsfeld, G. Xue, Z. Bao, Probing the interfacial molecular packing in TIPS-pentacene organic semiconductors by surface enhanced Raman scattering. *J. Mater. Chem. C* **2**, 2985–2991 (2014).
47. Z. Jiang, *GIXSGUI*: A MATLAB toolbox for grazing-incidence x-ray scattering data visualization and reduction, and indexing of buried three-dimensional periodic nanostructured films. *J. Appl. Cryst.* **48**, 917–926 (2015).
48. R. Noriega, J. Rivnay, K. Vandewal, F. P. V. Koch, N. Stingelin, P. Smith, M. F. Toney, A. Salleo, A general relationship between disorder, aggregation and charge transport in conjugated polymers. *Nat. Mater.* **12**, 1038–1044 (2013).
49. Y. Ito, A. A. Virkar, S. Mannsfeld, J. H. Oh, M. Toney, J. Locklin, Z. Bao, Crystalline ultrasmooth self-assembled monolayers of alkylsilanes for organic field-effect transistors. *J. Am. Chem. Soc.* **131**, 9396–9404 (2009).
50. C.-W. Chu, S.-H. Li, C.-W. Chen, V. Shrotriya, Y. Yang, High-performance organic thin-film transistors with metal oxide/metal bilayer electrode. *Appl. Phys. Lett.* **87**, 193508 (2005).
51. T. Buffeteau, F. S. Lagugné-Labarthet, C. Sourisseau, Vibrational circular dichroism in general anisotropic thin solid films: Measurement and theoretical approach. *Appl. Spectrosc.* **59**, 732–745 (2016).

Acknowledgments

Funding: This research was primarily supported by the National Science Foundation (NSF) EAGER grant under grant number NSF DMR 16-41854. J.J.K. and Y.D. acknowledge support of NSF CAREER award under grant number NSF DMR 18-47828. K.S.P. and Y.D. acknowledge partial support by the ONR under grant number N00014-19-1-2146. P.K. acknowledges the AAUW International Fellowship and partial support by the NSF MRSEC: Illinois Materials Research Center under grant number DMR 17-20633. This research used resources of The Advanced Photon Source, a U.S. Department of Energy (DOE) Office of Science User Facility operated for the DOE Office of Science by the Argonne National Laboratory under contract number DE-AC02-06CH11357. A part of this research was performed in the Frederick Seitz Materials Research Laboratory Central Facilities, University of Illinois. D.B., R.D., and Y.O. acknowledge support by the European Union's Horizon 2020 research and innovation program under grant agreement number 722651 (SEPOMO project). Computational resources were provided by the Consortium des Équipements de Calcul Intensif (CÉCI), funded by the Fonds de la Recherche Scientifique de Belgique (F.R.S.-FNRS), and the Tier-1 supercomputer of the Fédération Wallonie-Bruxelles, an infrastructure funded by the Walloon Region. J.M. and X.L. appreciate the support from the NSF (NSF CAREER award number 1653909). J.-K.L. and S.-H.J. thank the National Research Foundation of Korea (NRF) funded by the Ministry of Science and ICT (2018M3D1A1058536). **Author contributions:** K.S.P., J.J.K., and Y.D. designed the research project, and Y.D. supervised the project. K.S.P. carried out the experiments and analyzed the data. J.J.K. built the printing system and performed the COMSOL simulations and analysis. R.D. performed the molecular simulations under the supervision of Y.O. and D.B. G.Q. and P.K. performed the GIXD measurements. X.L. synthesized the semiconducting polymers (PII-2T, PTII-2T, and DPP2T-TT) under the supervision of J.M. S.-H.J. synthesized the semiconducting polymer (DPP-BTz) under the supervision of J.-K.L. K.S.P., J.J.K., and Y.D. wrote the manuscript. All authors discussed, revised, and approved the manuscript. **Competing interests:** The authors declare that they have no competing interests. **Data and materials availability:** All data needed to evaluate the conclusions in the paper are present in the paper and/or the Supplementary Materials. Additional data related to this paper may be requested from the authors.

Submitted 23 January 2019
Accepted 28 June 2019
Published 9 August 2019
10.1126/sciadv.aaw7757

Citation: K. S. Park, J. J. Kwok, R. Dilmurat, G. Qu, P. Kafle, X. Luo, S.-H. Jung, Y. Olivier, J.-K. Lee, J. Mei, D. Beljonne, Y. Diao, Tuning conformation, assembly, and charge transport properties of conjugated polymers by printing flow. *Sci. Adv.* **5**, eaaw7757 (2019).

Tuning conformation, assembly, and charge transport properties of conjugated polymers by printing flow

Kyung Sun Park, Justin J. Kwok, Rishat Dilmurat, Ge Qu, Prapti Kafle, Xuyi Luo, Seok-Heon Jung, Yoann Olivier, Jin-Kyun Lee, Jianguo Mei, David Beljonne and Ying Diao

Sci Adv **5** (8), eaaw7757.
DOI: 10.1126/sciadv.aaw7757